19th Australasian Fluid Mechanics Conference
Melbourne, Australia
8-11 December 2014

Spanwise Inclination and Meandering of Large-Scale Structures in a High-Reynolds-Number Turbulent Boundary Layer

W. J. Baars, K. M. Talluru*, B. J. Bishop, N. Hutchins and I. Marusic

Department of Mechanical Engineering
The University of Melbourne, Victoria 3010, Australia

Abstract

Surveys of the skin-friction velocity under a high-Reynolds-number turbulent boundary layer were conducted to obtain the imprint generated by large-scale structures in the logarithmic region. Two spanwise arrays of hot-films, separated in the streamwise direction, were employed to investigate the evolution of the large-scale footprint with the emphasis on usage for future real-time control. An estimate of the downstream footprint, based on the upstream input, is compared directly to the measurement from the second array. Firstly, Fourier decomposition and proper orthogonal decomposition reveal the spanwise homogeneity and periodicity. Then, by using Taylor's hypothesis as a first-principal estimate, the anticipated on/off-control for targeting high-speed structures is 68.3 % accurate in terms of timing. When only considering the spanwise modes that remain coherent, and their individual convective speeds, the accuracy is improved to 72.7 %. In the final part, we elucidate on the spanwise inclination and meandering of large-scale structures. It is shown how inclined structures do not drift in the spanwise direction in the conditionally averaged results.

Introduction

Past research on high-Reynolds-number turbulent boundary layers has revealed the existence of large-scale turbulent structures in the logarithmic region, consisting of flow regions where the instantaneous velocity is spatially coherent in the form of uniform momentum zones, which are either below or above the mean velocity [4, 13, 8]. The coherence is evidenced by their significant lifetimes in the streamwise direction (up to 20 δ) and organization in the spanwise and wall-normal direction [13]. An ongoing effort at the University of Melbourne is to actively control these large-scale structures. The motive for doing this relies on the fact that large-scale structures modulate the amplitude of near-wall velocity fluctuations [9, 12]. Henceforth, if we can efficiently target and reduce the high-speed structures, it is envisioned that near-wall shear-stress fluctuations, and its mean, will be reduced.

For non-intrusive, practical purposes, an array of skin-friction sensors was flush-mounted to the wall and formed our detection plant. The skin-friction footprint is generated by structures throughout the entire boundary layer, but, by implementing a real-time temporal filter, the large-scale footprint is retrieved (see Hutchins *et al.* [10] and others). As a first step, feedforward control is anticipated, and hence, a real-time implementation of this form of control requires a finite streamwise separation distance between the location of *detection* and the location where subsequent control *action* is executed. This follows from an accumulation of constraints imposed by real-time filtering, control decision making, mechanical delays and the physical inclination of large-scale structures. Since feedforward control relies on an estimate of the *action* imprint, a suitable estimation procedure, with the *detection* imprint taken as the input, has to be embraced for efficient control. In this work, two skin-friction arrays (positioned at locations of detection and action; visualized in figure 1) are employed to assess various estimation procedures. Here, we focus on the efficient usage of these techniques for real-time control, and so, the current work is an initial step towards implementation of feedforward control in an efficient manner.

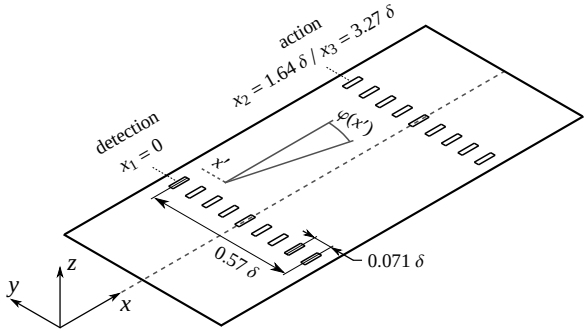

Figure 1. Schematic of two spanwise arrays (x_1 & x_2 or x_1 & x_3) of shear-stress sensors; an actuation array of wall-normal jets is positioned at x_2 during real-time control studies.

Applicable estimation procedures will condense to stochastic estimation, which has been widely applied in coherent turbulent flows. As a first-principal case, we will explore the estimate from a uniform convection velocity (Taylor's hypothesis). Then, first-order stochastic estimation techniques, dubbed Linear Stochastic Estimation (LSE) [1] are explored by applying single-time LSE (*e.g.* Cole and Glauser [6]). Additionally, data were decomposed in the spanwise direction using Proper Orthogonal Decomposition (POD) [11] and Fourier analysis to investigate the spanwise periodicity of the footprint. Such decompositions also allow us to perform an estimate of each individual mode. Here, a simple single-time estimate is performed and we refer to Bonnet *et al.* [5] for a more comprehensive approach by which low-dimensional estimates can be performed by combining LSE and POD; see also the overview provided by Baars and Tinney [2].

Experimental Arrangement

Experiments were conducted in the high Reynolds number boundary layer wind tunnel at the University of Melbourne at a friction Reynolds number of $Re_\tau = U_\tau\delta/\nu = 14,400$ (U_∞ = 20 m/s); where $\delta = 0.367$ m is the boundary layer thickness, $U_\tau = 0.64$ m/s is the friction velocity, and ν is the kinematic viscosity. Each spanwise array of shear-stress sensors consisted of nine flush-mounted Dantec 55R47 glue on type hot-films, with an equidistant spacing of $\Delta y/\delta = 0.071$ and a span of $L_y/\delta = 0.567$ (figure 1). The hot-films were operated in CTA mode, with an overheat ratio of 1.05, and were synchronously acquired at a rate of $f_s = 5$ kHz using AA labs AN 1003 anemometers. The sensors were calibrated such that the friction velocity in m/s was obtained [10]. Two streamwise separation distances

* Present address: Discipline of Mechanical Engineering, University of Newcastle, NSW 2308, Australia.

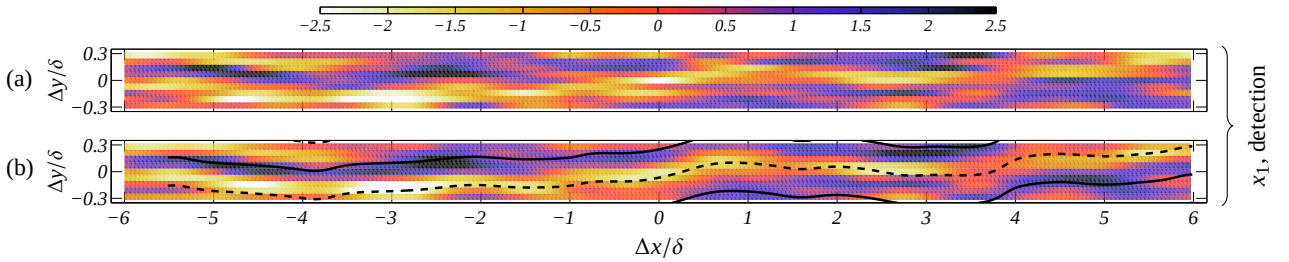

Figure 2. (a) Contour of fluctuating friction velocity at x_1, (b) reconstructed field using Fourier mode $m = 0$, 1 & 2. Contour levels correspond to: $U_\tau(x_1, \mathbf{y}, \Delta x) / \left(\sqrt{\Lambda}\sigma_\tau\right)$; where σ_τ is the standard deviation of the signal and $\Lambda = 1$ for (a) and $\Lambda = 0.727$ for (b).

of $x_2 - x_1 = 1.64\delta$ and $x_3 - x_1 = 3.27\delta$ were considered. The former represents a typical spacing between detection and jet actuation as encountered during real-time control, since we require a temporal interval on the order of $(x_2 - x_1)/U_c \approx 43$ ms. The convective speed $U_c^+ = 21.9$ was found from two-point correlations. After signal acquisition, a 1D Gaussian filter was convolved with each signal to retrieve the large-scale fluctuations; the standard deviation of the filtered field is $\sigma_\tau = 0.0507$ m/s. The Gaussian filter of 6 σ in length spanned $1.5 f_s \delta / U_c = 131$ samples. In the remainder of this work, wall-imprints are presented in terms of spatial coordinates. As an example, the Gaussian-filtered field at x_1, denoted as $U_\tau(x_1, \mathbf{y}, t)$, is visualized in figure 2a in terms of $U_\tau(x_1, \mathbf{y}, \Delta x)$, where $\Delta x = -tU_c$. Finally, data corresponding to $TU_\infty/\delta = 8.6 \cdot 10^5$ boundary layer turn-over times were used to obtain converged statistics at large wavelengths.

Spanwise Homogeneity and Periodicity of Footprint

A low-dimensional analysis of the friction velocity field is now conducted. The significance of doing this is to allow the variation in the spanwise direction to be described by a reduced set of time-dependent coefficients, since one can omit the spatial modes that possess insignificant amounts of energy, or discard modes that are incoherent in the streamwise direction. First we consider a Fourier decomposition at one particular location x_i; note that x_i is omitted in further expressions for convenience. The friction velocity field $U_\tau(\mathbf{y}, t)$ is decomposed according to

$$U_\tau(\mathbf{y}, t) = \sum_{m=0}^{4} c_m(t) e^{im\pi \mathbf{y}/l}, \tag{1}$$

where length $2l = 9/8 L_y$ and $c_m(t) \in \mathbb{C}$ are the Fourier coefficients. Equation (1) can be recast as a real-valued series, where real coefficients $\tilde{c}_{m'}(t) \in \mathbb{R}$ contribute as even ($m' \geqslant 1$) and odd modes ($m' \leqslant -1$); $\tilde{c}_0(t)$ remains similar and equals the time-varying spanwise mean. As opposed to Fourier decomposition, POD [11, 3] does not assume mode-shapes *a priori*. Generally, orthogonal spatial modes are deduced directly from an ensemble of coherent data, while time-dependent coefficients characterize the temporal dynamics of each mode. The classical form of the POD, applied in the spanwise direction results in

$$U_\tau(\mathbf{y}, t) = \sum_{n=1}^{9} a_n(t) \phi^{(n)}(\mathbf{y}). \tag{2}$$

The mode-shapes $\phi^{(n)}(\mathbf{y})$ are obtained by solving the following integral eigenvalue problem:

$$\int R(\mathbf{y}, \mathbf{y}') \phi^{(n)}(\mathbf{y}') d\mathbf{y}' = \lambda^{(n)} \phi^{(n)}(\mathbf{y}), \tag{3}$$

where $R(\mathbf{y}, \mathbf{y}') = \langle U_\tau(\mathbf{y}, t) U_\tau(\mathbf{y}', t) \rangle$ is the two-point correlation matrix. POD coefficients are obtained through the mapping

$$a_n(t) = \int U_\tau(\mathbf{y}, t) \phi^{(n)}(\mathbf{y}) d\mathbf{y}, \tag{4}$$

and their variance is equal to the associated eigenvalues $\lambda^{(n)}$. Hence, the total resolved energy (TRE) is given by

$$\Lambda = \sum_{m'=-4}^{4} \lambda^{(m')} = \sum_{n=1}^{9} \lambda^{(n)} = 9\sigma_\tau^2, \tag{5}$$

where $\lambda^{(m)}$ is the variance of Fourier coefficient $\tilde{c}_{m'}(t)$. The aforementioned techniques can be implemented in real-time, provided an initialization is performed to obtain the POD modes offline (solving equation 3).

Let us now elucidate the modal energy distributions. Pre-multiplied energy spectra of the mode coefficients are shown in figure 3a. The area covered by one spectrum is proportional to the fraction of energy in the corresponding mode. Figure 4 complements this by visualizing the fraction of energy $\alpha = \lambda/\Lambda$ per mode. Before discussing the spectral content it is important

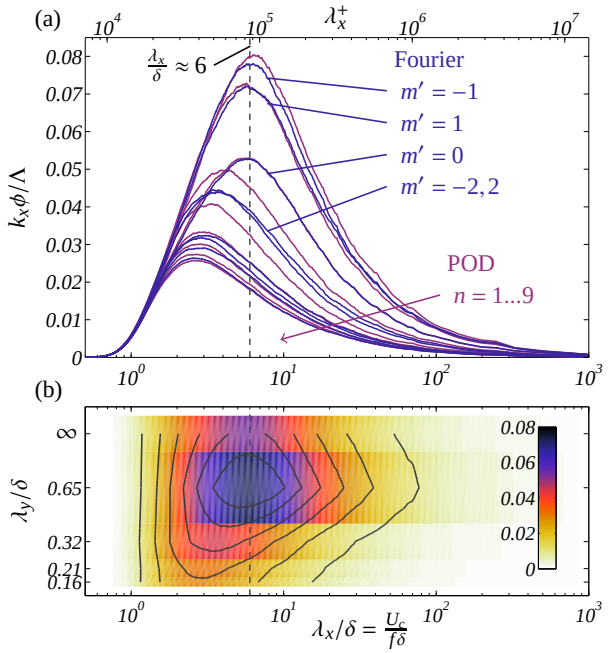

Figure 3. (a) Pre-multiplied energy spectra of time-varying coefficients $\tilde{c}_{m'}(t)$ and $a_n(t)$. (b) Two-dimensional energy spectrum of streamwise/spanwise friction-velocity fluctuations.

to comment on the mode-shapes, which are not shown in this condensed paper. POD modes $n = 1$ & 2 resemble a spanwise variation that is equal to the first odd and even Fourier modes, $m' = -1$ & 1, respectively; they also posses near-identical energy fractions. Furthermore, POD modes $n = 1$ & 2 have non-zero means, which suggests a coherent phase relation between Fourier modes $m' = 0$ & $m' = -1, 1$; however, this is beyond the scope of this paper. Nonetheless, the field is homogeneous

in y and a Fourier decomposition is justified. Fourier modes with higher rank m comprise smaller spanwise wavelengths and their discrete values can be deduced from the ordinate of figure 3b, where the 2D energy spectrum is shown. Evidence of the expected peak around $(\lambda_x,\lambda_y)/\delta = (6, 0.7)$ is there despite the sparse resolution in λ_y.

To illustrate the strength of a low-dimensional representation, the Gaussian filtered field in figure 2a is reconstructed by preserving Fourier modes $m = 0$, 1 & 2 (figure 2b). Essentially, the field is filtered in y by discarding the least energetic modes. Additionally, the phase angle between odd and even Fourier modes can be utilized to identify high-speed and low-speed streaks. The streaks corresponding to mode $m = 1$ are identified on the graph, which, by visual inspection identify the regions of high (–) and low (- -) skin-friction velocity reasonably well.

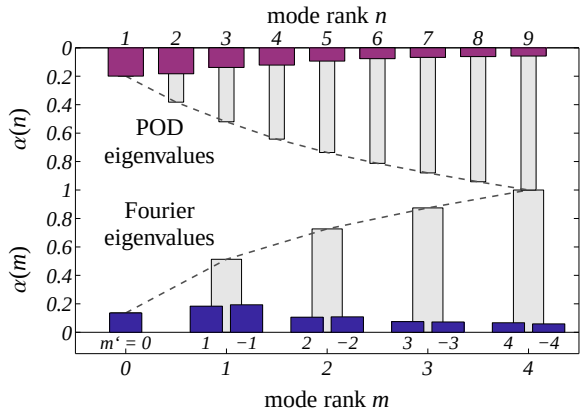

Figure 4. Energy fractions per mode: $\alpha = \lambda/\Lambda$.

Streamwise Estimation of Footprint

A first logical step in examining the evolution of the footprint is to consider its convective speed U_c. Figure 5 presents the convective speed (abscissa) obtained from the maximum in the two-point correlation (ordinate). First, this is performed for the Gaussian-filtered signals in a one-to-one fashion. Then, POD coefficients of the same rank are correlated: $a_n(x_1,t)$ with $a_n(x_i,t)|_{i=2,3}$, and similarly for the Fourier coefficients: $\tilde{c}_{m'}(x_1,t)$ with $\tilde{c}_{m'}(x_i,t)|_{i=2,3}$. For all cases, U_c is higher for an increasing separation distance ($\circ \rightarrow \square$), which is simply the consequence of larger scales remaining more coherent. The convective speeds are disparate for modes with different spanwise wavelengths. For example, the convective speed of Fourier mode $m = 2$ is $\approx 5\%$ smaller than its equivalent for modes $m = 0$ & 1. This implicitly shows the hierarchy of structures throughout the boundary layer, since wider and longer structures reside further from the wall, and hence, convect faster.

Since our aim during on/off-control is to exclusively target high-speed structures, we quantify the similarity between the estimate and direct measured field at x_2 as follows. The fraction of time that the estimated field $\hat{U}_\tau(x_2,\mathbf{y},t) > 0$, given the measured field $U_\tau(x_2,\mathbf{y},t) > 0$, is defined as β, *i.e.* in terms of set theory: $(\hat{U}_\tau > 0) \cap (U_\tau > 0)$; note that in the case of random firing $\beta = 50$ %, while $\beta = 100$ % for an ideal scenario. Furthermore, during all instances of misfiring, not all skin-friction events have equal and opposite amplitude compared to the instances of successful targeting. Therefore, the mean of the targeted events, relative to the mean of the positive skin-friction events at x_2, is used to quantify the amplitude of the targeted events: $\zeta = [\overline{U_\tau} \mid \hat{U}_\tau > 0]/[\overline{U_\tau} \mid U_\tau > 0]$. In the remainder we refer to β as the 'timing efficiency' and ζ as the 'targeting efficiency'.

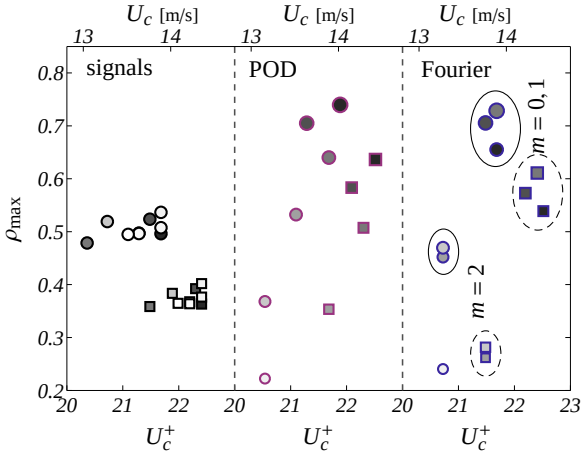

Figure 5. Two-point correlation maxima $\rho_{\max}$ with associated convective speeds for raw signals, POD- and Fourier-coefficients (both separation distances $x_2 - x_1$: $\circ$ & $x_3 - x_1$: $\square$).

As a first principal estimate we apply a uniform convection velocity (Taylor's hypothesis) to the field at x_1 (input) to obtain the wall print (output) at x_2. This scenario is case A in table 1.

case	U_c^+ [m/s]	β [%]	ζ [%]	$\overline{U_\tau} \mid U_\tau > 0$
A	21.3	68.3	51.8	0.79
B	21.3	72.6	64.5	0.81
C	21.7 / 21.6 / 20.7	72.7	64.6	0.81

Table 1. Similarity between estimate and direct measured field at downstream location x_2.

Next, we only consider Fourier modes that remain coherent over the streamwise distance considered (see figure 5). The field at x_1 is reconstructed using Fourier mode $m = 0,1$ & 2 and shifted to location x_2 according to its mean convective speed ($U_c^+ = 21.3$). For illustrative purposes, the estimated and measured field at x_2 are shown in figures 6a and 6c, respectively, alongside their binary maps of targeting instances. The fraction of overlap of the gray portions of figures 6b and 6d (for all available data) is equal to $\beta = 72.6$ %; the similarity parameters are listed in table 1, case B. As a logical consequence of a decrease in misfiring, the targeting efficiency is increased to $\zeta = 64.5$ %.

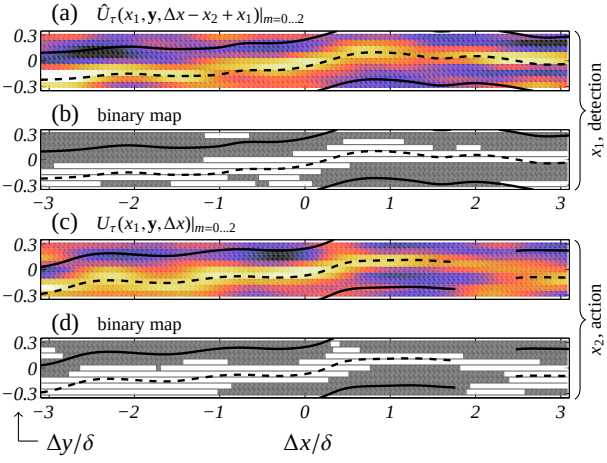

Figure 6. (a,c) Visualization of the reconstructed estimated field at location x_2 (based on input at x_1) and measured field at x_2, by omitting streamwise incoherent Fourier modes $m = 3$ & 4, with alongside (c,d) the associated binary maps of firing instances in grey.

Finally, the attempt is made to increase the accuracy of the estimate in case B by considering the convective speed associated with each distinct mode. The individual convective speeds are listed for case C in table 1. It is clear that the improvement in the estimate is negligible, which can be easily explained. The difference in convective speeds, and the associated shifts for the estimate, is relatively small compared to the length of the large-scale structures, and so, the improvement will only be more significant when larger streamwise distances are considered. This however, comes at the expense of a decrease in coherence. It is important to realize that a perfect estimate ($\beta = \zeta = 100$ %) is practically impossible. First of all, structures dissipate and have a limited lifetime, and secondly, structures might appear from outside the domain. Nonetheless, we believe that an overall efficiency taken as $\eta = 2/\left(\beta^{-1} + \zeta^{-1}\right) = 68.4$ % (case B or C) should result in an effective form of control.

Meandering and Spanwise Inclination

In order to investigate the spanwise inclination and drift of structures we reside to the phase angle of paired Fourier modes, as was used in figure 2b to identify low- and high-speed streaks. The footprint at x_1 is conditioned on events where the spanwise inclination angle of Fourier mode $m = 1$ obeys by $\varphi(x_1) > 15°$; here we take the midpoint of a structure and the result is shown in figure 7a. Skin-friction fields at downstream locations x_2 and x_3 are conditionally averaged using the same condition $\varphi(x_1) > 15°$ in order to reveal how the inclined structures appear downstream (figures 7b and 7c). The inclined structures are shown to relax downstream since they become less inclined and less pronounced in amplitude. Furthermore, the structure remains centered at $y = 0$, which shows that the inclined structures do not drift in a preferred spanwise direction, on average. The implication of this is that corrections for spanwise drift in the estimate have to be more novel than being based on an instantaneous spanwise inclination of the structure.

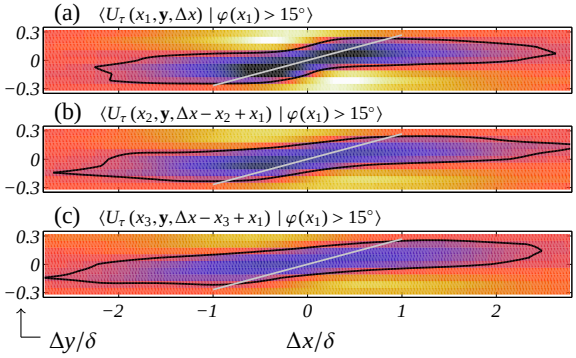

Figure 7. (a) Skin-friction velocity footprint at x_1 conditioned on spanwise inclination angles $\varphi(x_1) > 15°$, and associated conditioned footprints (shifted by $U_c^+ = 21.3$) at location x_2 (b) and x_3 (c); the white lines indicate a 15° spanwise inclination.

Conclusions

Estimates of the time-dependent spanwise skin-friction velocity footprint under a high-Reynolds-number turbulent boundary layer were performed. The estimation-input was acquired at a *detection* location, where after the estimated field at a downstream distance of $x_2 - x_1 = 1.64\ \delta$ was compared with a direct measurement. When only considering the spanwise Fourier modes being coherent over this distance, the instances of high-speed events were targeted 72.7 % accurate. An ongoing effort at the University of Melbourne is to control high-speed large-scale structures, and so, an array of wall-normal jets will be positioned at the downstream location to perform control *action*.

More accurate *streamwise evolution* can be accounted for in future work using the implementation of multi-time (spectral) LSE per mode if time-constraints of the real-time control set-up allow for this. Variation in the spanwise drift, or meandering of the structures, is more difficult to account for, as it was shown that on average, spanwise inclined structures do not move in the spanwise direction. Henceforth, a possible scheme to account for *spanwise drift* is not trivial to implement. Finally, the mode decomposition generates a wide variety of control strategies that will be explored.

Acknowledgements

Funding for this study was graciously provided by the Australian Research Council.

References

[1] Adrian, R.J., Conditional eddies in isotropic turbulence, *Phys. Fluids*, **22**, 1979, 2065–2070.

[2] Baars, W.J. and Tinney, C.E., Proper orthogonal decomposition-based spectral higher-order stochastic estimation, *Phys. Fluids*, **26**, 055112, 2014.

[3] Berkooz, G., Holmes, P. and Lumley, J.L., The proper orthogonal decomposition in the analysis of turbulent flows, *Annu. Rev. Fluid Mech.*, **25**, 1993, 539–575.

[4] Blackwelder, R.F. and Kovasznay, L.S.G., Time scales and correlations in a turbulent boundary layer, *Phys. Fluids*, **15**, 1972, 1545–1554.

[5] Bonnet, J.P., Cole, D.R., Delville, J., Glauser, M.N. and Ukeiley, L.S., Stochastic estimation and proper orthogonal decomposition: complementary techniques for identifying structure, *Exp. Fluids*, **17**,1994, 307–314.

[6] Cole, D.R. and Glauser, M.N., Applications of stochastic estimation in the axisymmetric sudden expansion, *Phys. Fluids*, **10**, 1998, 2941–2949.

[7] Dennis, D.J.C and Nickles, T.B., Experimental measurement of large-scale three-dimensional structures in a turbulent boundary layer. Part 1. Vortex packets, *J. Fluid Mech.*, **673**, 2011, 180–217.

[8] Hutchins, N. and Marusic, I., Evidence of very long meandering structures in the logarithmic region of turbulent boundary layers, *J. Fluid Mech.*, **579**, 2007, 1–28.

[9] Hutchins, N. and Marusic, I., Large-scale influences in near-wall turbulence, *Phil. Trans. R. Soc. A*, **365**, 2007, 647–664.

[10] Hutchins, N., Monty, J.P., Ganapathisubramani, B., Ng, H.C.H. and Marusic, I., Three-dimensional conditional structure of a high-Reynolds-number turbulent boundary layer, *J. Fluid Mech.*, **673**, 2011, 255–285.

[11] Lumley, J.L., The structure of inhomogeneous turbulent flows, *Atmospheric Turbluence and Radio Wave Propagation*, eds. Yaglom, A.M. and Tatarski, V.I., Nauka, Moscow, Russia, 1967, 166–178.

[12] Marusic, I., Mathis, R. and Hutchins, N., Predictive model for wall-bounded turbulent flow, *Science*, **329**(5988), 2010, 193–196.

[13] Tomkins, C.D. and Adrian R.J., Spanwise structure and scale growth in turbulent boundary layers, *J. Fluid Mech.*, **490**, 2003, 37–74.